Article

Electrocatalytic N–C–N coupling over a hierarchically ordered open single-atom superstructure toward organonitrogen synthesis

Yingchun He[1,2,3], Dong-Dong Ma[1], Ke Ma[1], Xiaofang Li[1], Lili Han [1,3], Xin-Tao Wu[1,2,3] & Qi-Long Zhu [1,2,4] ✉

Electrochemically constructing C–N and N–C–N bonds provides an economical and sustainable alternative to conventional chemosynthesis. Herein, a hierarchically ordered open superstructure of N-doped carbon isolated with accessible three-coordinated Zn single-atom sites is explored for efficient electrocatalytic N–C–N coupling. Benefiting from the distinctive structural merits, this catalyst enables electrocatalytic preparation of N–C–N bonded compounds from methanol and amines. Notably, the Faradaic efficiency and selectivity of *N,N,N',N'*-tetramethyldiaminomethane reach up to 77% and 96% at 0.8 V, respectively. Further integrating the aminoalkylation reaction, an electro-thermo cascade synthesis is explored with the electrochemically obtained *N,N,N',N'*-tetramethyldiaminomethane serving as a unique reagent, leading to a specific set of organonitrogen compounds with (dimethylamino) methyl substituent, including topotecan hydrochloride, an anti-tumor drug, with a high yield of 95%. Furthermore, the in situ spectroscopic characterization and calculations unveil that the under-coordinated Zn-N_3 sites play a pivotal role in stabilizing the key *CH_2O intermediate, thereby facilitating subsequent nucleophilic addition with amines.

Controlled chemical bond formation is a cornerstone of modern chemical synthesis, as it allows for the precise construction of complex molecules with desired properties. The ability to selectively form and break bonds for precise synthesis of targeted chemicals under mild conditions has far-reaching implications for fields like pharmaceuticals, where product purity, efficiency, and cost are critical. Common approaches for bond formation include photocatalysis[1,2], thermocatalysis[3,4], and electrocatalysis[5,6]. Among these, electrocatalytic bond formation stands out owing to its mild reaction conditions, eco-friendly nature, and high selectivity[7,8]. Additionally, it allows fine-tuned control over the reaction process by adjusting parameters

such as potential and current density, making it a versatile tool for sustainable chemical synthesis[9,10].

Methanol, often referred to as "liquid sunshine", is a clean energy source and crucial feedstock that can be synthesized through the hydrogenation of carbon dioxide with hydrogen derived from solar energy[11,12]. With methanol as the primary chemical and electricity as the driving force, the C–N, C–C, and C–O bonds can be constructed efficiently and greenly[13–16]. As shown in Fig. 1, Shao et al. reported the synthesis of formamide (with C–N bonds) in an undivided cell from methanol and ammonia with B-doped diamonds as the electrocatalyst[17]. Xia et al. selectively synthesized ethylene glycol (with

[1]State Key Laboratory of Structural Chemistry, Fujian Institute of Research on the Structure of Matter, Chinese Academy of Sciences, Fuzhou, China. [2]Fujian Science & Technology Innovation Laboratory for Optoelectronic Information of China, Fuzhou, China. [3]University of Chinese Academy of Sciences, Beijing, China. [4]School of Materials Science and Engineering, Zhejiang Sci-Tech University, Hangzhou, China. ✉e-mail: qlzhu@fjirsm.ac.cn
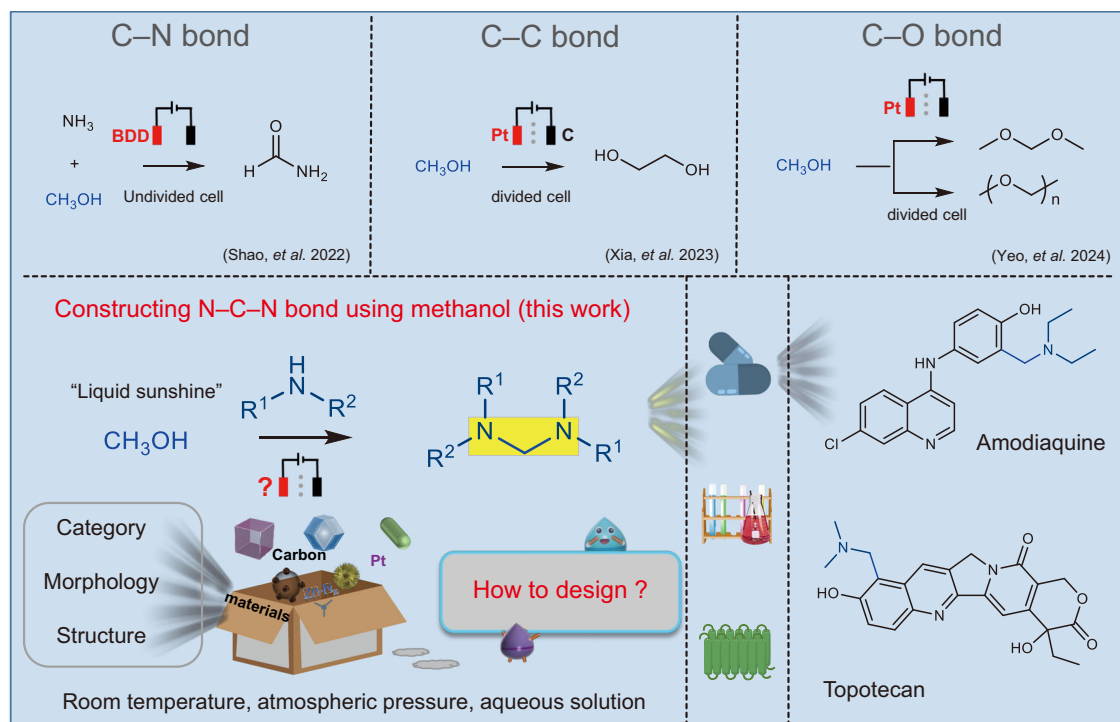
Fig. 1 | Schematic of electrochemical and electro-thermo cascade approaches for methanol valorization. Electrochemical strategies for the construction of diverse chemical bonds using methanol as a reagent and the electro-thermo cascade synthesis of the organonitrogen compounds with (dimethylamino)methyl substituent using the N−C−N bonded compounds as the specific reagents. R^1 and R^2 represent different or identical groups.

C−C bonds) from methanol using Pt as the electrocatalyst[18]. More recently, Yeo et al. efficiently constructed the C−O bonds, leading to a series of formaldehyde derivatives[19]. However, to the best of our knowledge, the electrochemical construction of N−C−N bonds using methanol as a reagent has not yet been explored. We also summarized the works on the electrosynthesis of other organonitrogen compounds from C- and N-containing small molecules (Supplementary Table 1).

The controlled formation of N−C−N bonds is of particular significance, which is a key building block in a range of applications from drug development to materials science[20,21]. However, the formation of N−C−N bonds is challenging due to the inherent difficulty in controlling the reactivity of nitrogen-containing species, which often leads to side reactions and poor selectivity. By leveraging electrocatalytic techniques, we aim to overcome the traditional obstacles in N−C−N bond formation, providing a green and efficient pathway for producing the valuable organonitrogen compounds with high selectivity. Moreover, the N−C−N bonded compounds can be further applied to synthesize the high-value organonitrogen compounds with (dimethylamino)methyl substituent through the aminoalkylation reaction[22]. Consequently, by exploring the electro-thermo cascade synthesis strategy, it is possible to synthesize important organonitrogen compounds, including the anti-tumor drugs such as topotecan hydrochloride with low non-hematologic toxicity[23].

The efficient formation of specific chemical bonds through electrocatalysis depends on the elaborate design and synthesis of advanced electrocatalysts, as the category, morphology, and structure of the catalysts significantly impact their catalytic performance[24–27]. Among these commonly used catalysts, the single-atom catalysts (SACs) are becoming exceptionally promising catalysts due to their unique catalytic performance resulting from maximum atomic efficiency, unsaturated metal coordination structures, and electron confinement[28–30]. Compared to other transition metals (e.g., Fe, Co, Ni) based SACs, the Zn-SACs have been much less studied for

electrocatalysis because of their unusual electronic structures and relatively lower reactivity[31,32]. Nevertheless, this characteristic of the Zn-SACs could allow for the controlling of the reaction steps for generating and accumulating the specific intermediates. It has been extensively reported that methanol can readily convert into formic acid/formate through deep electrooxidation over transition metal-based electrocatalysts[33]. Thus, we propose that the Zn-SACs with moderate intrinsic oxidizability would be helpful to stabilize the $^*CH_2O$ intermediate, avoiding over electrooxidation of methanol, which can be further attacked by amine nucleophilic reagents to form the C−N bonds. On the other hand, compared to the $Zn-N_4$ configuration with symmetric coordination and electronic structure, the under-coordinated Zn atoms (e.g., $Zn-N_3$) could lead to a more unsaturated coordination environment, thus optimizing the electronic structure to enhance the catalytic properties[34,35]. Furthermore, the exposure of the active sites and mass and charge transfer are crucial factors for optimizing the efficiency of electrocatalysis. In particular, the hierarchically ordered porosity with multi-scale pores in an orderly manner can significantly enhance the performance of electrocatalysts, where the micropores can increase the surface area to fully expose the active sites, while the mesopores and macropores aid in reducing the diffusion resistance of reactants and products, particularly for the relatively larger organic molecules, and simultaneously act as reaction reservoirs for boosting reactions[36,37]. Meanwhile, the ordered pore engineering could form periodic microelectric fields to promote the reactant diffusion, thus effectively optimizing the reaction kinetics[38]. Inspired by the above factors, the construction of a under-coordinated Zn-SAC with hierarchically ordered porous structure may offer potential for efficient electrocatalytic synthesis of organonitrogen compounds using primary chemicals like methanol.

Herein, a unique Zn-SAC (Zn_1/h-OPNC) featuring hierarchically ordered open N-doped carbon isolated with dispersed under-coordinated $Zn-N_3$ sites has been developed for efficient electrochemical construction of N−C−N bonds. The hierarchically ordered open superstructure of such electrocatalyst significantly improves the
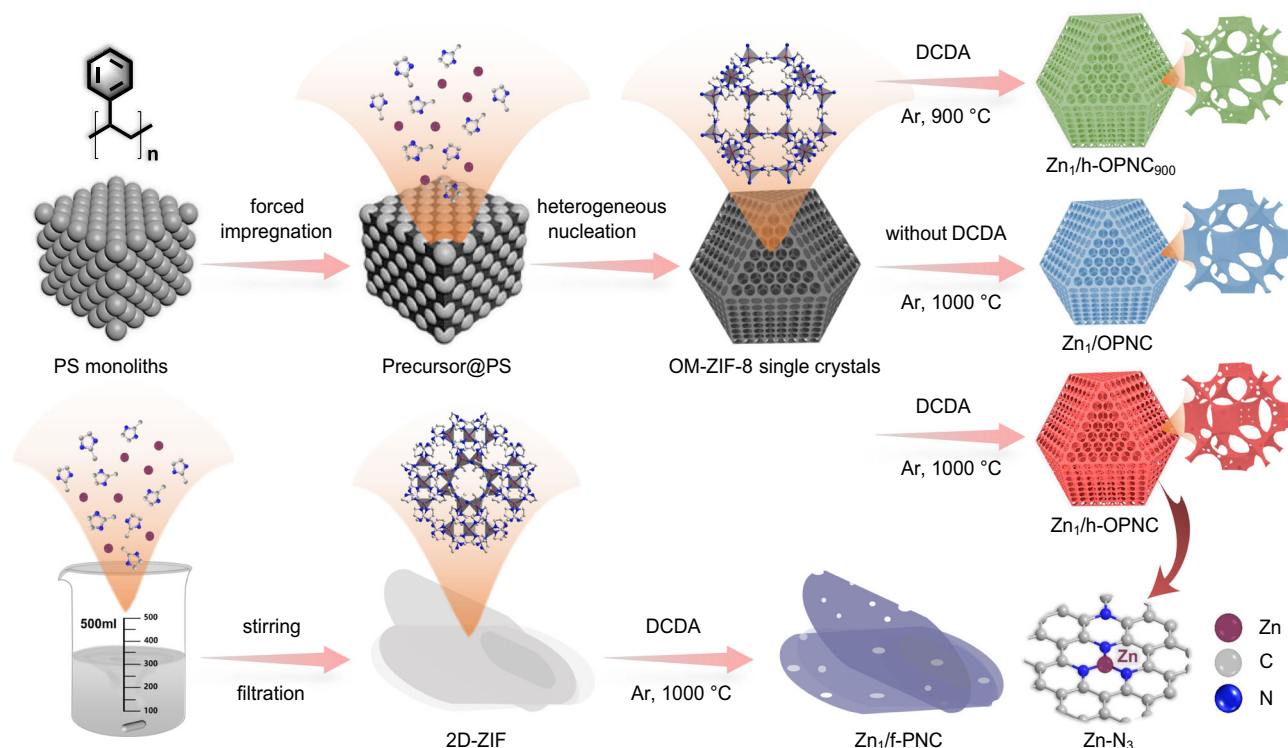
Fig. 2 | Schematic illustration of the synthesis procedures for the Zn-SACs with diverse nanostructures. The monoliths of densely arranged polystyrene (PS) microspheres are used as the template for the preparation of OM-ZIF-8 single crystals. Zn_1/h-$OPNC_{900}$ and Zn_1/h-OPNC exhibit similar hierarchically ordered open superstructures, while Zn_1/OPNC features an ordered open superstructure, and Zn_1/f-PNC consists of thin porous nanosheets.

accessibility of the under-coordinated Zn single-atom sites and reduces mass and charge transfer resistance. Consequently, the distinctive structural characteristics of Zn_1/h-OPNC facilitate the efficient electrocatalytic production of N−C−N bonded *N,N,N′,N′*-tetramethyldiaminomethane (TMDM) from methanol and dimethylamine (DMA), achieving a high productivity of 357 μmol h^{-1} cm^{-2}, along with a near-quantitative selectivity of 96% and a high Faradaic efficiency (FE_{TMDM}) of 77% at 0.8 V. Furthermore, an electro-thermo cascade synthesis process is accommodated using TMDM as the specific reagent for the aminoalkylation reaction, leading to the efficient synthesis of a range of high-value organonitrogen compounds with (dimethylamino)methyl substituents, including topotecan hydrochloride, an anti-tumor drug, with an isolated yield up to 95% on a gram scale. In situ attenuated total reflection infrared (ATR-IR) spectroscopy and density functional theory (DFT) calculations indicate that undercoordinated $Zn-N_3$ sites facilitate methanol oxidation and stabilize the key *CH_2O intermediate, which then reacts with amine via nucleophilic attack. This work guides the rational design of the spatial and atomic site structures of electrocatalysts and the electrochemical building of N−C−N bonds for valuable organonitrogen synthesis.

Results

Synthesis and characterization of catalysts

Figure 2 illustrates the schematic diagrams for the preparation of three catalysts derived from ordered macroporous ZIF-8 (OM-ZIF-8) single crystals using the monoliths of polystyrene (PS) spheres as the template. In summary, the three-dimensional (3D) ordered PS monoliths were initially prepared through the self-assembly of PS spheres with a diameter of 300 nm (Supplementary Fig. 1). Then, the methanol solutions of zinc nitrate and 2-methylimidazole were mixed and added to the PS monoliths, and the solution was allowed to fully access the template voids by forced impregnation. The methanol-ammonia mixture was further added to promote the nucleation of ZIF-8. After reaction, the template was removed to obtain the single crystals of

OM-ZIF-8 with a 3D interconnected ordered macro-microporous structure (Supplementary Fig. 2). Finally, the Zn_1/h-$OPNC_{900}$ and Zn_1/h-OPNC, which feature similar hierarchically ordered superstructures with macro-, nano-, and micropores, were obtained by the pyrolysis of the OM-ZIF-8 precursor mixed with dicyandiamide (DCDA) in an argon atmosphere at 900 and 1000 °C, respectively. By contrast, the consistent procedure without the addition of DCDA resulted in a lack of the multilevel pores in the derived Zn_1/OPNC, which was predominantly characterized by macro- and micropores. To facilitate a more comprehensive comparison of the advantages offered by the hierarchically ordered open superstructure morphology, we also synthesized 2D-ZIF with a two-dimensional nanosheet morphology with a thickness of ~1.13 nm (Fig. 2, Supplementary Figs. 3 and 4). Furthermore, the thin porous N-doped carbon nanosheets isolated with Zn single-atom sites (Zn_1/f-PNC) were synthesized using 2D-ZIF mixed with DCDA as the precursor.

During the pyrolysis of the ZIF-8 precursors, nitrogen-rich DCDA served as a pore-forming agent and nitrogen source, which decomposed at temperatures between 300 and 350 °C, producing a substantial quantity of ammonia and other N-containing gases to etch the ZIF-8 skeleton and thus induce the formation of additional mesopores. On the other hand, when the temperature was increased above 900 °C, although a significant quantity of Zn in ZIF-8 sublimated due to the low boiling point of metallic Zn (907 °C), a considerable portion of Zn remained and dispersed in the form of single atoms within the carbon skeleton. Consequently, these processes resulted in the unique open superstructure of Zn_1/h-OPNC with hierarchically ordered porous N-doped carbon isolated with dispersed Zn single-atom sites. Figure 3a, b, e−f, and Supplementary Fig. 5a, b, f−g present the scanning electron microscope (SEM) images of Zn_1/h-OPNC, Zn_1/OPNC, Zn_1/h-$OPNC_{900}$, and Zn_1/f-PNC at different magnifications, respectively. As illustrated in Fig. 3a, e, and Supplementary Fig. 5a, all three catalysts well inherited the morphology of the maternal OM-ZIF-8 single crystals, showing the approximate polyhedra with highly ordered
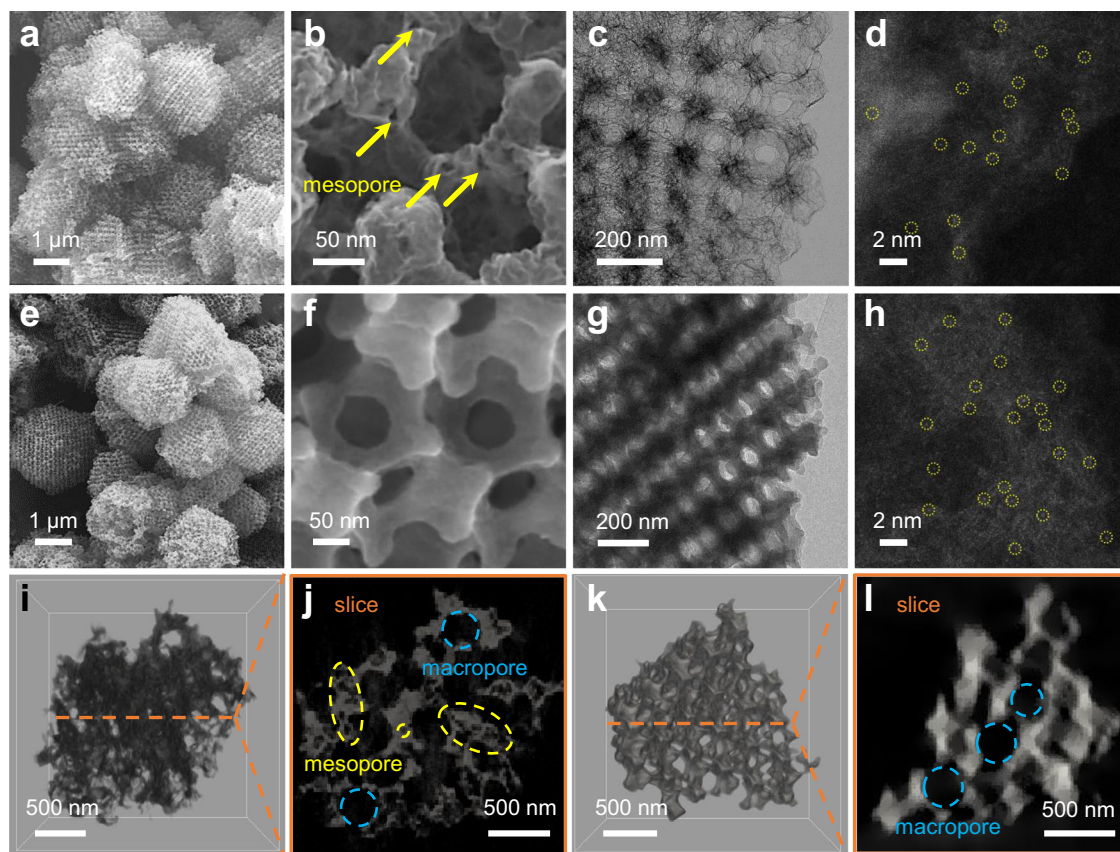
Fig. 3 | Morphological and structural characterization of Zn$_1$/h-OPNC and Zn$_1$/ OPNC. SEM images of (**a**, **b**) Zn$_1$/h-OPNC, (**e**, **f**) Zn$_1$/OPNC. TEM images of (**c**) Zn$_1$/h-OPNC, (**g**) Zn$_1$/OPNC. AC-HADDF-STEM images of (**d**) Zn$_1$/h-OPNC, (**h**) Zn$_1$/OPNC. 3D TEM tomography: 3D TEM images of (**i**) Zn$_1$/h-OPNC and (**k**) Zn$_1$/OPNC; cross-section images of (**j**) Zn$_1$/h-OPNC and (**l**) Zn$_1$/OPNC. Zn atoms are partially circled in yellow for highlight in (**d**) and (**h**).

macropore arrangement, where the average macropore diameter is about 120 nm and the thickness of the surrounding walls is about 30 nm. Notably, for both Zn$_1$/h-OPNC and Zn$_1$/h-OPNC$_{900}$, in addition to the original ordered macroporous skeleton structures, a substantial quantity of mesopores are distributed uniformly throughout the carbon skeletons (Fig. 3b and Supplementary Fig. 5b), forming the hierarchically ordered open superstructures. Such distinctive structures could play vital roles in electrocatalysis by facilitating the mass transfer within the conductive networks, enhancing the exposure of active sites and acting as the micro/nanoreactors to enrich substrates. In contrast, the SEM images of Zn$_1$/OPNC reveal an ordered macroporous structure, lacking mesopores observed in these skeletons (Fig. 3f). Besides, Zn$_1$/f-PNC exhibits a thin nanosheet nanostructure with some macropores (Supplementary Fig. 5f, g).

The transmission electron microscopy (TEM) images of the four catalysts provide further evidence that Zn$_1$/h-OPNC and Zn$_1$/h-OPNC$_{900}$ exhibit ordered macro- and mesoporous morphological characteristics, while Zn$_1$/OPNC displays an ordered macroporous morphological feature and Zn$_1$/f-PNC exhibits ultrathin two-dimensional nanosheet morphology (Fig. 3c, g and Supplementary Fig. 5c, h). The energy-dispersive X-ray (EDX) elemental mappings demonstrate that the C, N, and Zn elements are present in a uniform distribution across the four catalysts (Supplementary Fig. 5d, i and Supplementary Fig. 6), and the contents of Zn were detected by inductively coupled plasma (ICP) in Supplementary Table 2. The aberration-corrected high-angle annular dark-field scanning transmission electron microscopy (AC-HADDF-STEM) images show the existence of a considerable number of bright spots (partially circled in yellow for highlight), indicating that these Zn atoms are uniformly distributed in a single-atom level on the carbon skeleton of the four

catalysts, without discernible agglomeration (Fig. 3d, h, and Supplementary Fig. 5e, j).

To clearly visualize the hierarchical porous morphology of Zn$_1$/ OPNC, the 3D TEM tomography was further conducted. As shown in Fig. 3i, k, Supplementary Fig. 7 and Supplementary Movie 1 and 2, it is observed that both Zn$_1$/h-OPNC and Zn$_1$/OPNC retain the ordered macroporous morphological feature. Notably, the cross-section images depicted in Fig. 3j, l display the apparent mesoporous structure of Zn$_1$/h-OPNC (partially circled in yellow for emphasis), in addition to the macropores. By contrast, the relatively large mesopores were not observed for Zn$_1$/OPNC. Furthermore, Zn$_1$/h-OPNC exhibits a 58% increase in porosity in comparison to Zn$_1$/OPNC on the basis of the TEM tomographic results (Supplementary Fig. 8), providing further evidence that Zn$_1$/h-OPNC forms the hierarchically ordered open superstructure.

To gain further insights into the nanostructures of these Zn-SACs, more other characterizations were conducted. As illustrated in Fig. 4a, the powder X-ray diffraction (PXRD) patterns of the four catalysts only exhibit a characteristic crystalline phase of graphitic carbon devoid of metal peaks, which further corroborates the atomic dispersion of the metal Zn. Furthermore, the comparable intensity ratios of the D-band and G-band (I_D/I_G) in the Raman spectra of the four catalysts indicate a similar degree of graphitization and surface defects (Fig. 4b). The hierarchical porous structures of the catalysts can be further corroborated by N$_2$ sorption analysis. As shown in Supplementary Fig. 9, the N$_2$ sorption isotherms of Zn$_1$/h-OPNC, Zn$_1$/h-OPNC$_{900}$, and Zn$_1$/OPNC exhibit a combination of I and IV-type isotherms, displaying a high N$_2$ uptake at lower pressures and distinctive hysteresis loops at higher pressures. This suggests the existence of both micropores and mesopores in the three catalysts, which is further verified by the pore size
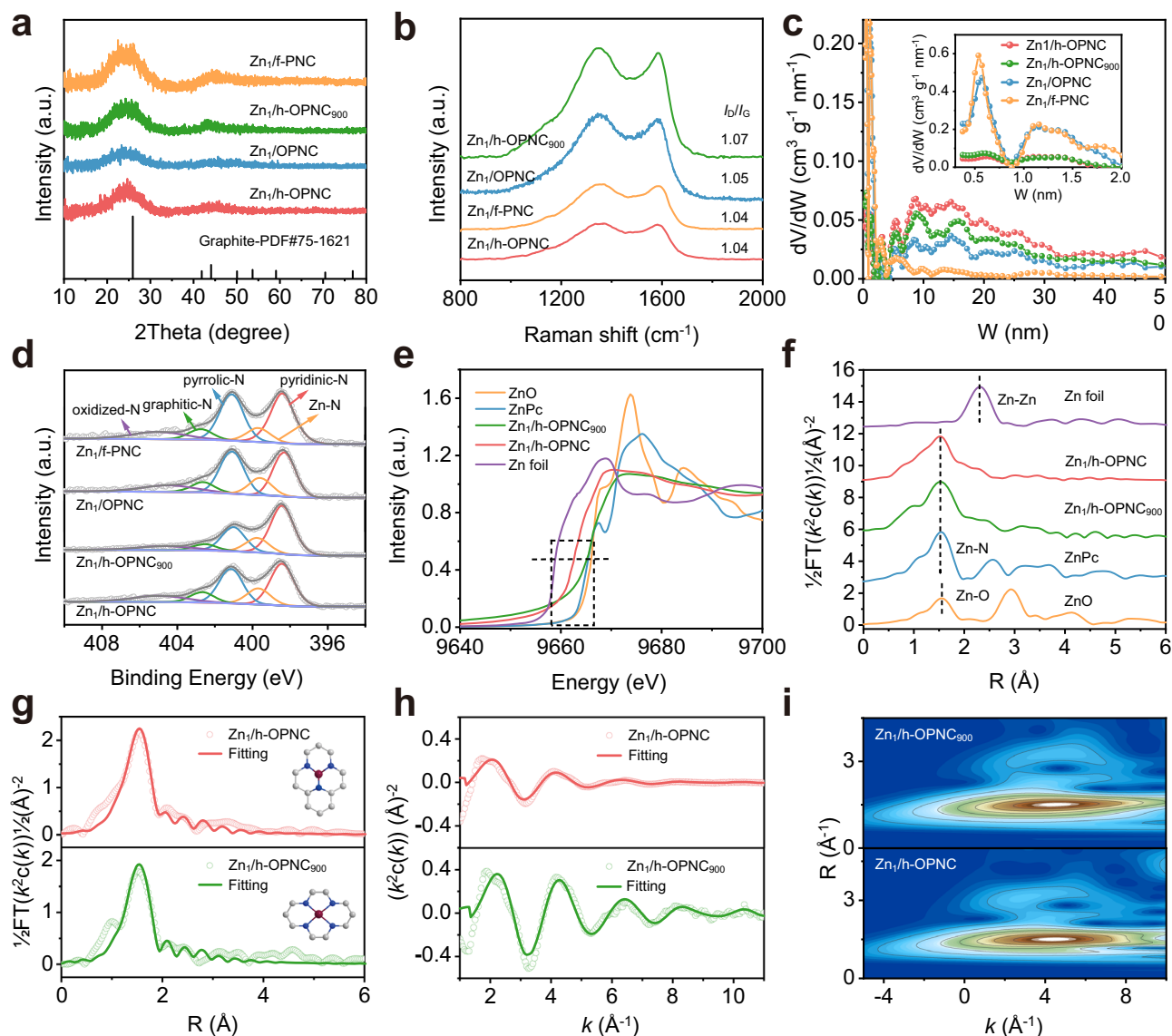
Fig. 4 | Physical characterizations of Zn₁/h-OPNC, Zn₁/h-OPNC₉₀₀, Zn₁/OPNC and Zn₁/f-PN. a PXRD patterns; (**b**) Raman spectra; (**c**) pore size distribution curve; (**d**) high-resolution N 1*s* XPS spectra; (**e**) XANES spectra; (**f**) FT-EXAFS spectra; FT-EXAFS fitting curves in (**g**) *R* space and (**h**) *k* space; (**i**) WT-EXAFS plots of Zn₁/h-OPNC and Zn₁/h-OPNC₉₀₀. The insets in (**g**) show the Zn-N₃ (top) and Zn-N₄ (bottom) models, respectively.

distribution curves (Fig. 4c). However, the proportions of the mesopores in Zn₁/h-OPNC and Zn₁/h-OPNC₉₀₀ are higher than that of Zn₁/OPNC. As a result, the abundance of the multilevel porosity of Zn₁/h-OPNC leads to a high Brunauer–Emmett–Teller (BET) surface area of $460.72 \, m^2 \, g^{-1}$. Furthermore, Zn₁/f-PNC displays a typical type I isotherm, indicative of the predominance of micropores. These findings align well with their SEM and TEM observations. Then, the X-ray photoelectron spectroscopy (XPS) technique was employed to elucidate the chemical compositions and chemical status of the catalysts. As shown in Fig. 4d, the high-resolution N 1*s* spectra can be deconvoluted into five distinct types of N species, corresponding to pyridine N (398.5 eV), pyrrole N (401.2 eV), graphite N (402.7 eV), oxide N (404.5 eV), and Zn-N (399.7 eV). In the high-resolution Zn 2*p* spectra, two peaks were observed at 1044.8 and 1021.9 eV, which are assigned to Zn $2p_{1/2}$ and Zn $2p_{3/2}$, respectively (Supplementary Fig. 10)[34,39]. The XPS analysis indicates that all these Zn-SACs possess the Zn-Nₓ coordination.

To further investigate the coordination environment and chemical information of the Zn atoms in the catalysts, X-ray absorption near edge structure (XANES) and extended X-ray fine structure spectroscopy (EXAFS) analysis were performed. As illustrated in Fig. 4e, within the energy range of 9658 to 9666 eV, the Zn K-edge XANES spectrum of Zn₁/h-OPNC is situated between those of Zn foil and ZnO, indicating that the valence state of the Zn sites is between 0 and +2. By contrast, the spectrum of Zn₁/h-OPNC₉₀₀ is close to that of the Zn(II) phthalocyanine (ZnPc) reference, suggesting the different coordination and electronic structures between Zn₁/h-OPNC and Zn₁/h-OPNC₉₀₀ obtained at different calcination temperatures. Furthermore, the Fourier transformed (FT)-EXAFS spectra of Zn K-edge (Fig. 4f), reveal that the predominant peaks for Zn₁/h-OPNC and Zn₁/h-OPNC₉₀₀ are at ~1.53 Å, which could be attributed to the first coordination shell of Zn-N bonding. No typical peaks for Zn-Zn bonding at ~2.30 Å were detected, further confirming the formation of the Zn-Nₓ sites. Moreover, the chemical coordination environments of Zn₁/h-OPNC and Zn₁/h-OPNC₉₀₀ were determined through EXAFS fitting (Fig. 4g, h). The fitting results in *R* space and *k* space indicate that the Zn-N coordination numbers of Zn₁/h-OPNC and Zn₁/h-OPNC₉₀₀ are around 3 and 4, respectively (Supplementary Table 3), corresponding to the Zn-N₃ and Zn-N₄ sites. To ascertain the coordination environments of Zn₁/h-OPNC and Zn₁/h-OPNC₉₀₀ more visually, the wavelet
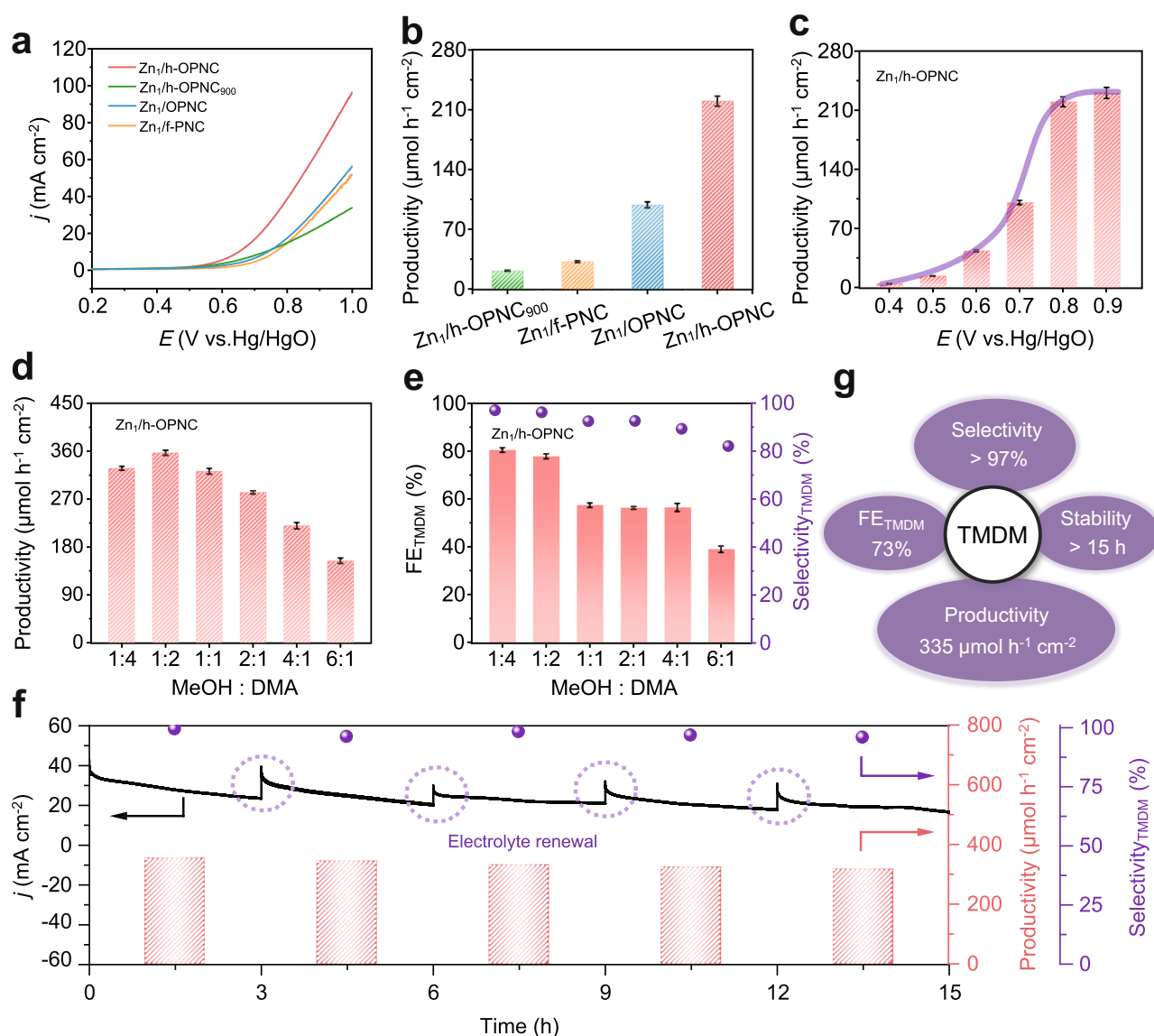
Fig. 5 | Electrocatalytic properties of Zn₁/h-OPNC, Zn₁/h-OPNC₉₀₀, Zn₁/OPNC and Zn₁/f-PNC for N–C–N coupling to prepare TMDM. a LSV curves and (**b**) productivity at 0.8 V in 0.7 M K₂CO₃ with MeOH:DMA = 4:1; (**c**) productivity of Zn₁/h-OPNC at different potentials in 0.7 M K₂CO₃ with MeOH:DMA = 4:1; (**d**) productivity and (**e**) FE$_{TMDM}$ of Zn₁/h-OPNC at 0.8 V in 0.7 M K₂CO₃ with different concentration ratios of MeOH and DMA; (**f**) stability test for Zn₁/h-OPNC at 0.8 V in 0.7 M K₂CO₃ with MeOH:DMA = 1:2; (**g**) overall performance diagram for stability test.

transform (WT) of the EXAFS spectra was conducted (Fig. 4i and Supplementary Fig. 11). The results demonstrate that the maximum intensities of Zn₁/h-OPNC and Zn₁/h-OPNC₉₀₀ at -3.89 and -4.02 Å⁻¹, respectively, are attributed to the Zn-N bonds, and no Zn-Zn peaks were observed at ~7.8 Å[40,41]. The above characterization results demonstrate that the Zn₁/h-OPNC catalyst featuring a hierarchically ordered open superstructure isolated with readily accessible undercoordinated Zn-N₃ sites has been successfully synthesized.

Electrocatalytic N–C–N coupling to prepare TMDM and its derivatives

In view of the unique nanostructure of Zn₁/h-OPNC and the catalytic Zn-N₃ sites, we employed it as a catalyst for electrocatalytic N–C–N coupling to synthesize special organonitrogen compounds from methanol and amines. Taking the electrosynthesis of TMDM as an example, we initially evaluated the electrocatalytic activity and selectivity of Zn₁/h-OPNC, Zn₁/h-OPNC₉₀₀, Zn₁/OPNC, and Zn₁/f-PNC for the preparation of TMDM using methanol and dimethylamine (DMA) in the H-type cell. The linear

sweep voltammetry (LSV) curves of these catalysts are presented in Fig. 5a, demonstrating that Zn₁/h-OPNC exhibits the lowest onset potential and the highest current density, while Zn₁/OPNC and Zn₁/f-PNC display moderate current densities, and Zn₁/h-OPNC₉₀₀ exhibits the lowest one. The results should be associated with the morphological configurations of the four catalysts, as well as the coordination environments of the Zn single-atom sites. By normalizing the current densities of the catalysts to their electrochemically active surface areas (ECSAs) (Supplementary Fig. 12a-e), the ECSA-normalized LSV curves were obtained. As shown in Supplementary Fig. 12f, the normalized current density of Zn₁/h-OPNC is significantly higher than that of Zn₁/h-OPNC₉₀₀, indicating that the Zn-N₃ sites exhibit a better intrinsic catalytic activity in comparison to Zn-N₄. During the electrocatalysis processes, gas chromatography mass spectrometer (GC-MS), gas chromatography (GC), and nuclear magnetic resonance (NMR) spectroscopy were employed for qualitatively and quantitatively analyzing the products (Supplementary Figs. 13–15). As illustrated in Fig. 5b, consistent with the current

density tendency observed in Fig. 5a, Zn_1/h-OPNC exhibits the highest productivity of TMDM, reaching 220 $\mu mol\ h^{-1}\ cm^{-2}$, while those over Zn_1/OPNC, Zn_1/f-PNC, and Zn_1/h-OPNC$_{900}$ are 98.56, 32.06, and 21.43 $\mu mol\ h^{-1}\ cm^{-2}$, respectively. This considerable discrepancy in performance could be attributed to their different nanostructures. Compared with Zn_1/OPNC$_{900}$, Zn_1/h-OPNC has a unique hierarchically ordered open superstructure, in which the plentiful well-ordered macropores, mesopores, and micropores can effectively facilitate mass transfer and sufficiently expose the Zn-N_3 active sites. Meanwhile, in comparison to Zn_1/f-PNC with an ultrathin nanosheet morphology beneficial to the site exposure, the voids with ordered arrangement in Zn_1/h-OPNC can act as the micro/nanoreactors with a nanoconfinement effect, which enables the enrichment of the substrates in an optimal manner and the stabilization of the intermediates, thereby facilitating the subsequent N–C–N coupling reaction[42,43]. A substrate adsorption experiment was performed to provide further evidence for the hypothesis that the hierarchically ordered open superstructure can enrich the substrates (Supplementary Table 4). Furthermore, as Zn_1/h-OPNC and Zn_1/h-OPNC$_{900}$ possess similar morphology and porosity, their activity disparity can elucidate the higher intrinsic electrocatalytic activity of the Zn-N_3 active sites with lower coordination than that of the Zn-N_4 sites. It is important to note that the moderate activity of Zn-N_3 active sites, in comparison to other transition metal (e.g., Pt, Co, Ni) based SACs[44–46], can avoid the deep electrooxidation of methanol to formate or CO_2 and facilitate the formation and accumulation of the $*CH_2O$ intermediates, thereby favoring further attacked by amine nucleophilic reagents to form the N–C–N bonds.

As illustrated in Fig. 5c and Supplementary Fig. 16, it was observed that as the reaction potential increased, the productivity of TMDM exhibited a quick rise until it reached a plateau at 0.8 V, whereas the selectivity and FE$_{TMDM}$ exhibited a decline with the emergence of by-products such as formate and N,N-dimethylformamide (DMF). It is notable that within the test potential range, the formate is trace and only a small quantity of TMDM underwent further oxidation to form DMF, which was further demonstrated by single-variable electrolysis experiments (Supplementary Table 5). This indicates that the Zn-N_3 sites are capable of stabilizing the $*CH_2O$ while remaining inert to TMDM, thereby promoting the generation of TMDM. Collectively, these observations indicate that the optimal reaction potential is 0.8 V. Subsequently, the impact of varying the methanol and DMA concentrations in the reaction electrolyte on TMDM generation was investigated. When the methanol-to-dimethylamine ratio was 1:2, TMDM could be generated at the highest productivity of 357 $\mu mol\ h^{-1}\ cm^{-2}$ with a FE$_{TMDM}$ of 77% and a near-quantitative selectivity of 96% (Fig. 5d, e and Supplementary Fig. 17). The FE$_{TMDM}$ was found to be only 7.6% when only DMA was added, while a trace amount of DMF was generated, indicating that methanol is a necessary substrate for generating a large amount of TMDM (Supplementary Table 5). As illustrated in Supplementary Fig. 18, the catalytic performance of Zn_1/h-OPNC was superior to those of Zn_1/OPNC, Zn_1/f-PNC, and Zn_1/h-OPNC$_{900}$ under the optimal test conditions (MeOH:DMA = 1:2, 0.8 V). This indicates that the distinctive structure and atomic sites of Zn_1/h-OPNC exert a facilitating effect on the reaction. Furthermore, the long-term stability test for 15 h demonstrates that Zn_1/h-OPNC exhibited a consistent catalytic activity, capable of well maintaining the high FE$_{TMDM}$ (-73%), productivity (-335 $\mu mol\ h^{-1}\ cm^{-2}$), and selectivity (-97%) for TMDM production (Fig. 5f, g).

In light of the remarkable efficacy of Zn_1/h-OPNC in the electrocatalytic synthesis of TMDM, we proceeded to construct a series of N–C–N bonded compounds from methanol by introducing different amines. As shown in Fig. 6a and Supplementary Figs. 19–21, the replacement of dimethylamine with N-me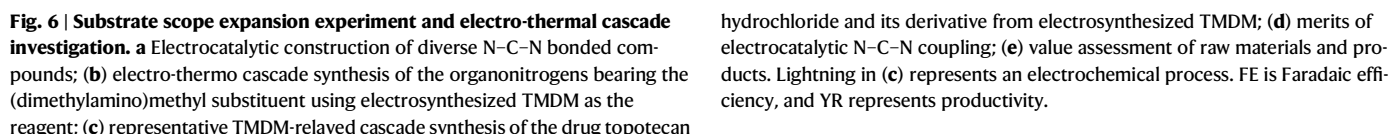thylethylamine, diethylamine, and morpholine allowed for the electrosynthesis of N,N′-diethyl-N,N′-dimethylmethanediamine (FE: 47%, YR: 135 $\mu mol\ h^{-1}\ cm^{-2}$), N,N,N′,N′-tetraethylmethanediamine (FE: 31%, YR: 28 $\mu mol\ h^{-1}\ cm^{-2}$) and dimorpholinomethane (FE: 12%, YR: 21 $\mu mol\ h^{-1}\ cm^{-2}$), respectively. It can be reasonably assumed that the steric-hindrance effect is responsible for the observed decline in yields and FEs of the N–C–N bonded products, due to the increased chain lengths of the amines and the introduction of the heterocycle. Furthermore, the scope of amines was expanded upon (Supplementary Fig. 22), yet the target N–C–N bonded products were not obtained. This may be due to the steric-hindrance effect and/or varied abilities of amines for subsequent nucleophilic addition.

Aminoalkylation reaction as an efficient approach for the introduction of C–C and C–N bonds, playing an important role in the field of organic synthesis, particularly medicinal chemistry. By virtue of the remarkably high productivity and selectivity for TMDM production over Zn_1/h-OPNC, we further proposed the electro-thermo cascade synthesis of a specific set of high-value organonitrogen compounds using the electrochemically generated TMDM as the reagent for aminoalkylation reaction (Fig. 6b and Supplementary Figs 23–30). Notably, all of these TMDM-relayed cascade reactions for the synthesis of the organonitrogens bearing the (dimethylamino)methyl substituent afforded the satisfactory yields exceeding 70%. Furthermore, this electro-thermo cascade synthesis strategy can be applied for synthesizing the expensive pharmaceuticals through introducing the (dimethylamino)methyl substituent. Taking topotecan hydrochloride as an example—an antitumor drug known for its low non-hematological toxicity and high cost, the reaction of 1.00 g of 10-hydroxycamptothecin with electrosynthesized TMDM produced 1.16 g of topotecan hydrochloride, corresponding to an excellent yield of 95% with the electron efficiency of 73% (Fig. 6c and Supplementary Figs. 31–33). In addition, the synthesized topotecan hydrochloride can be further reacted with 1,3-propanesulfonate, giving the topotecan derivative with a sulfonic acid group (Fig. 6c and Supplementary Figs. 34–36). This drug derivative with charges can be assembled into a nanomedicine, which has the potential to be an efficacious antitumor drug[47].

The aforementioned experimental results demonstrate that the production of diverse N–C–N bonded compounds is feasible through the alteration of the amine type using methanol as a cost-effective and environmentally benign raw material. To illustrate, the employment of DMA as the reagent enables the extraction of TMDM, a much more value-added product, through a straightforward process. Furthermore, the integration of electrosynthesis of TMDM with the aminoalkylation reaction can facilitate the electro-thermo cascade synthesis of special and high value-added organonitrogen products with the (dimethylamino)methyl substituent, which is a convenient procedure and is a promising strategy for large-scale applications (Fig. 6d). A further comparison is conducted between the prices of the feedstocks (methanol and dimethylamine), the potential by-products (formic acid and dimethoxymethane), and the product (TMDM) (Fig. 6e). The results indicate that TMDM exhibits the highest value, suggesting that the synthesis of TMDM from methanol and dimethylamine is economically feasible.

Mechanistic study

To delve into the reaction mechanism of the electrochemical N–C–N coupling over Zn_1/h-OPNC, the synthesis of TMDM from methanol and DMA was selected as a case study. Initially, the in situ attenuated total reflection infrared (ATR-IR) spectroscopy was employed to monitor the evolution of the intermediates during the reaction (Fig. 7a and Supplementary Fig. 37). The infrared spectra were recorded at 0.2 V for real-time analyzes. Firstly, no discernible characteristic peaks were detected at 0 s, suggesting that the reaction is an electrochemical process. At the 30-s mark, two distinctive negative and positive peaks emerged at 1415 and 1662 cm^{-1}, corresponding to the stretching modes of desorbed CO_3^{2-} and generated $*CH_2O$, respectively[48,49]. As the

Fig. 6 | Substrate scope expansion experiment and electro-thermal cascade investigation. a Electrocatalytic construction of diverse N–C–N bonded compounds; (**b**) electro-thermo cascade synthesis of the organonitrogens bearing the (dimethylamino)methyl substituent using electrosynthesized TMDM as the reagent; (**c**) representative TMDM-relayed cascade synthesis of the drug topotecan hydrochloride and its derivative from electrosynthesized TMDM; (**d**) merits of electrocatalytic N–C–N coupling; (**e**) value assessment of raw materials and products. Lightning in (**c**) represents an electrochemical process. FE is Faradaic efficiency, and YR represents productivity.

reaction time increased, the peak of $^*CH_2O$ at $1662\ cm^{-1}$ steadily rose until the 510-s mark, indicating that the amount of $^*CH_2O$ generated from the oxidation of methanol exhibited a growth tendency before reaching a plateau with increasing time. Moreover, a new peak emerged at $1623\ cm^{-1}$, which can be ascribed to the stretching vibration of $^*O=C-N$, indicating the decomposition of partial TMDM to yield DMF. Furthermore, in situ Raman spectroscopy was employed to record the evolution of the intermediates during the reaction (Supplementary Figs. 38 and 39). A series of comaparative experiments with variable substrates was conducted. As illustrated in Supplementary Fig. 39a, the addition of DMA alone did not result in the appearance of a signal at $1059\ cm^{-1}$ for $^*CH_2O$ during the 770 s electrolysis[50]. The $^*CH_2O$ peak was observed after 470 s of electrolysis when CH_3OH was the only reactant (Supplementary Fig. 39b). Furthermore, the addition of both CH_3OH and DMA resulted in the emergence of a distinct $^*CH_2O$ peak after only 170 s of electrolysis (Supplementary Fig. 39c). This suggests that the addition of DMA can facilitate the oxidation of methanol, resulting in the formation of $^*CH_2O$. When $^{13}CH_3OH$ was employed, a new peak emerged at $1020\ cm^{-1}$, which can be deduced as the peak of $^{*13}CH_2O$ (Supplementary Fig. 39d). The blue-shift of the $^*CH_2O$ peak can be ascribed to the isotope effect[51]. It is noted that the simultaneous presence of the $^{*12}CH_2O$ peak could be due to the reaction of OH^- in the electrolyte with DMA during the prolonged

electrolysis to produce $^{*12}CH_2O$[49]. The observation is consistent with the results of the univariate experiments (Supplementary Table 5), where only DMA was added and the FE_{TMDM} was 7.6%. Supplementary Fig. 40 shows the GC spectrum following the in situ Raman test, and the peak of the product TMDM is relatively weak due to the short electrolysis time of the in situ Raman test. The in situ ATR-IR and in situ Raman results demonstrate that the process of N–C–N coupling should be highly correlative with the oxidation of methanol to generate the key $^*CH_2O$ intermediate, which is followed by the aldimine condensation reaction through the nucleophilic addition with DMA.

To further support the critical role of the $^*CH_2O$ intermediate for TMDM production, we examined the GC profiles of the electrolytes following a series of reactions. As illustrated in Fig. 7b, when methanol and DMA were directly mixed in the electrolyte without energization, no TMDM was generated. Besides, the absence of TMDM in the reaction between formic acid and DMA suggests that the deep oxidation of methanol is unfavorable for TMDM preparation. Moreover, when formaldehyde was mixed with dimethylamine, although TMDM was produced, a considerable number of impurities were present, in comparison with the electrochemically prepared TMDM. The aforementioned results indicate that the electrochemical generation and stabilization of $^*CH_2O$ are essential for the subsequent nucleophilic addition reaction with DMA to generate TMDM. As a result, the
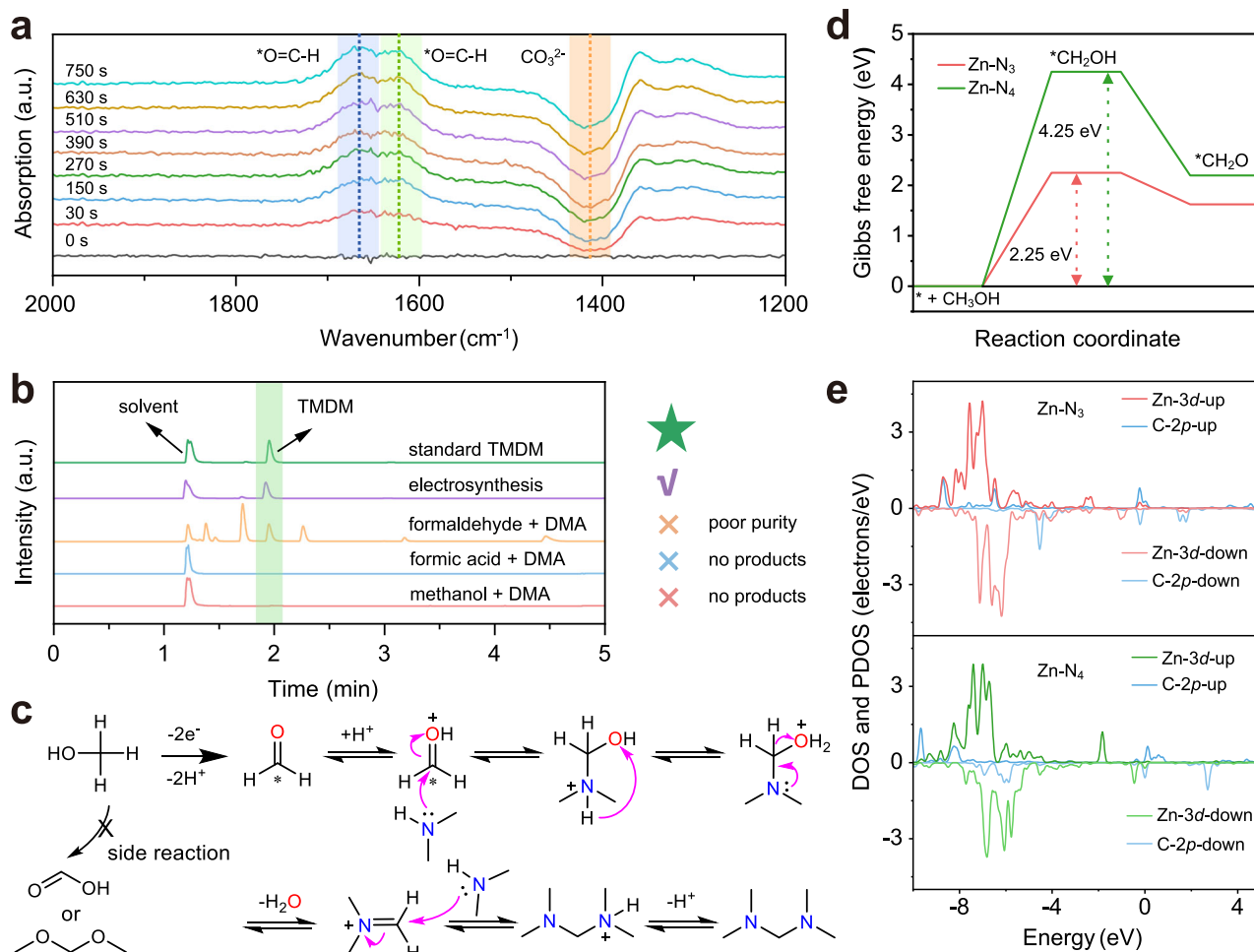
Fig. 7 | Mechanistic study and DFT calculations. a In situ ATR-IR spectra for the electrosynthesis of TMDM from methanol and DMA over Zn_1/h-OPNC; (**b**) control experiments for the synthesis of TMDM; (**c**) schematic representation of the electrosynthesis of TMDM; (**d**) Gibbs free energy for the formation of $*CH_2O$ over the $Zn-N_3$ and $Zn-N_4$ model configurations; (**e**) projected density of states (PDOS) for Zn-3d orbitals and C-2p orbitals of $*CH_2O$.

electrochemical preparation of TMDM exhibits a distinct advantage in terms of high purity. In light of the aforementioned experimental results, we summarized the reaction pathways. As illustrated in Fig. 7c, methanol is subjected to a moderate electrochemical oxidation process, resulting in the generation of $*CH_2O$, which subsequently undergoes a two-step nucleophilic addition reaction with DMA in the electrolyte, leading to the production of TMDM. As the applied potential increases, a small portion of TMDM undergoes further electrooxidation to form DMF, which is confirmed by univariate experiments (Supplementary Table 5). We deduce a proposed reaction mechanism for the electrosynthesis of TMDM from methanol and DMA in Supplementary Fig. 41.

Owing to the essential role of $*CH_2O$ during the electrochemical N–C–N coupling, the Gibbs free energy diagram for the $*CH_2O$ formation from methanol is presented over the $Zn-N_3$ and $Zn-N_4$ model configurations of Zn_1/h-OPNC and Zn_1/h-OPNC$_{900}$, repectively (Fig. 7d and Supplementary Fig. 42). Compared to the $Zn-N_4$ active sites, the $Zn-N_3$ ones display a lower change in Gibbs free energy, suggesting that the Zn_1/h-OPNC catalyst should be more conducive for the generation of $*CH_2O$. This conclusion is consistent with the experimental results, which demonstrate the superior performance of Zn_1/h-OPNC for producing TMDM than Zn_1/h-OPNC$_{900}$. Additionally, the projected density of states (PDOS) further reveals that the $Zn-N_3$ coordination structure of Zn_1/h-OPNC shows more overlap between the Zn-3d orbital and the C-2p orbital of $*CH_2O$, as compared to the $Zn-N_4$ of Zn_1/h-OPNC$_{900}$ (Fig. 7e). This also suggests that Zn_1/h-OPNC is

more favorable for the stabilization of $*CH_2O$, thereby facilitating the subsequent nucleophilic addition reaction of the amine.

Discussion

In summary, a hierarchically ordered open superstructure of N-doped carbon embedded with readily accessible under-coordinated $Zn-N_3$ sites has been constructed for efficient construction of N–C–N bonds. The integration of additional secondary mesopores into the ordered macroporous skeleton results in a distinctive superstructure that exhibits greatly enhanced site accessibility and mass transfer. In conjunction with the unique catalyst nanostructure and the highly exposed unusual $Zn-N_3$ sites, Zn_1/h-OPNC demonstrates high activity and selectivity for electrochemical N–C–N coupling. Particularly, TMDM, as a typical N–C–N bonded compound, can be efficiently generated with an ultrahigh productivity of 357 μmol h^{-1} cm^{-2}, as well as a near-unity selectivity of 96% and a high FE of ~77% at 0.8 V. Based on the efficient electrochemical N–C–N coupling, we successfully further developed the exemplary electro-thermo cascade strategy for TMDM-relayed synthesis of high-value organonitrogen compounds with (dimethylamino)methyl substituent, including gram-scale topotecan hydrochloride, an anti-tumor drug, with a high yield of 95%. Meanwhile, in situ ATR-IR spectroscopy and DFT calculations demonstrate that Zn_1/h-OPNC with under-coordinated $Zn-N_3$ sites facilitates the oxidation of methanol to produce the key $*CH_2O$ intermediate, thereby promoting subsequent nucleophilic addition step with amines. This work offers valuable guidance for the intelligent

design of advanced electrocatalysts and the electrochemical synthesis of organonitrogen compounds.

Methods

Materials

Styrene (99%) was obtained from Aladdin Co., and further washed by sodium hydroxide (NaOH, 10 wt%) aqueous solution and deionized water several times to remove the *p*-tert-butylcatechol. Potassium persulfate ($K_2S_2O_8$, A.R., Sinopharm Chemical Reagent Co. (SCRC)) was recrystallized before use. Polyvinyl pyrrolidone (PVP, M_w ~ 58000, Adamas), zinc nitrate hexahydrate ($Zn(NO_3)_2 \cdot 6H_2O$, A.R., SCRC), 2-methylimidazole ($C_4H_6N_2$, 98%, Aladdin Co.), methanol (CH_3OH, A.R., SCRC), Pt foil (Pt, Wuhan Gaoshiruilian Science and Technology Co.), carbon paper (CP, Toray Industries, Inc), ethanol (CH_2CH_3OH, A.R., SCRC), ammonium hydroxide ($NH_3 \cdot H_2O$, A.R., SCRC), *N,N*-dimethylformamide (C_3H_7NO, A.R., Xilong Technology), dicyandiamide ($C_2H_4N_4$, A.R., SCRC), dimethylamine (C_2H_7N, A.R., Shanghai Adamas Reagent Co., 40 wt.% solution in water), *N,N,N′,N′*-tetramethyldiaminomethane ($C_5H_{14}N_2$, RG., Shanghai Adamas Reagent Co.), dichloromethane (CH_2Cl_2, A.R., SCRC), 1,2-dichlorobenzene ($C_6H_4Cl_2$, A.R., SCRC), trichloromethane ($CHCl_3$, A.R., SCRC), phenol (C_6H_6O, A.R., SCRC), cuprous chloride (CuCl, A.R., SCRC), 2-naphthol ($C_{10}H_8O$, AG., Shanghai Adamas Reagent Co.), toluene (C_7H_8, A.R., SCRC), 1,2,4-triazole ($C_2H_3N_3$, AG., Shanghai Adamas Reagent Co.), palladium diacetylacetonate ($C_{10}H_{16}O_4Pd$, AG., Shanghai Adamas Reagent Co.), imidazole ($C_3H_4N_2$, AG., Shanghai Adamas Reagent Co.), succinic anhydride ($C_4H_4O_3$, AG., Shanghai Adamas Reagent Co.), 10-hydroxycamptothecin ($C_{20}H_{16}N_2O_5$, AG., Shanghai Adamas Reagent Co.), 1,3-propanesulfonate ($C_3H_6O_3S$, AG., Shanghai Adamas Reagent Co.), methanol-13C ($^{13}CH_3OH$, A.R., Shanghai Adamas Reagent Co.) were used without further purification.

Preparation of polystyrene (PS) monolith

0.5 g of PVP and 100 mL of deionized water were added in a 250 mL of three-necked flask and heated to 70 °C at 600 rpm under N_2 atmosphere. 13 mL of treated styrene was added and kept at 70 °C for 20 min. Then, 20 mL of 0.015 g mL^{-1} $K_2S_2O_8$ solution was added, and the reaction was continued for 24 h. The obtained suspension was centrifuged and dried at 60 °C to yield the PS monolith.

Preparation of OM-ZIF-8

First, the methanol solutions of $Zn(NO_3)_2 \cdot 6H_2O$ (22.5 mL, 0.36 g mL^{-1}) and 2-methylimidazole (22.5 mL, 0.30 g mL^{-1}) were prepared. After thoroughly mixing the above solutions, 4.0 g of PS template was added, and the mixture was impregnated for 30 minutes. Subsequently, the mixture was further vacuum degassed for 20 min. The PS template was taken out and dried at 50 °C for 6 h, and then transferred to 30 mL of methanol and ammonia (v:v = 1:1). The mixture was further vacuum degassed for 10 min and set aside for 24 h at room temperature to promote the growth of ZIF-8. Then, the soaked PS template was extracted and dried at 50 °C to obtain ZIF-8@PS. Finally, the PS template was removed by soaking in DMF, and the solid left was filtrated, rinsed with methanol, and dried to obtain OM-ZIF-8.

Preparation of Zn₁/h-OPNC, Zn₁/OPNC and Zn₁/h-OPNC₉₀₀

Zn_1/h-OPNC was obtained by calcining the mixture of OM-ZIF-8 (100 mg) and DCDA (500 mg) at 1000 °C for 2 h under an Ar atmosphere, with an elevated temperature rate of 2 °C min^{-1}. Zn_1/h-OPNC$_{900}$ and Zn_1/OPNC were prepared in the same way, except that Zn_1/h-OPNC$_{900}$ was calcined at 900 °C, while Zn_1/OPNC was calcined without adding DCDA.

Preparation of 2D-ZIF

0.330 g (1.11 mmol) of $Zn(NO_3)_2 \cdot 6H_2O$ and 0.985 g (12.0 mmol) of 2-methylimidazole were each dissolved in 90 mL of deionized water.

The above two solutions were mixed and stirred at room temperature for 24 h. After standing, the mixture was centrifuged, and the solid was rinsed with methanol and deionized water, and dried at 60 °C to obtain 2D-ZIF.

Preparation of Zn₁/f-PNC

Zn_1/f-PNC was obtained by calcining the mixture of 2D-ZIF (100 mg) and DCDA (500 mg) at 1000 °C for 2 h under an Ar atmosphere, with an elevated temperature rate of 2 °C min^{-1}.

Characterizations

The scanning electron microscopy (SEM) images were obtained on JSM6700-F. Powder X-ray diffraction (PXRD) patterns were gained on a MiniFlex diffractometer (MiniFlex600, Rigaku). Transmission electron microscopy (TEM) images and high-resolution transmission electron microscopy (HRTEM) images were collected from FEI Titan Themis 200. Atomic force microscope images were obtained in a Bruker Dimension ICON. The X-ray photoelectron spectroscopy (XPS) data were obtained from the Thermo Fisher ESCALAB 250Xi spectrometer. In situ attenuated total reflection-infrared (ATR-IR) spectra were recorded on the NICOLET 6700 instrument. The nuclear magnetic resonance (NMR) spectra were recorded on the ECZ600R. The liquid products were detected by Shimadzu GCMS-QP2020 gas chromatograph mass spectrometer (GC-MS) and Shimadzu GC-2018 gas chromatography (GC) featuring an FID detector and HP-5 column. The mass spectrometry (MS) spectra were recorded on the Bruker Impact II Q-TOF instrument.

3D TEM tomography

3D TEM tomography was collected from JEOL JEM-F200 at 200 kV. The electron micrographs were acquired using a single-axis high-tilt tomography holder from −73° to 71° with a linear tilt step of 2°. At each tilt angle, the beam was focused on a neighboring area to minimize the damage to the region of interest. The application of tophat filtering served to eliminate the back bottom and thereby mitigate the back bottom effect. The manual segmentation method was employed to divide the projection and extract the effective area. Image alignment was performed using the center of mass method. The aligned tilt series were reconstructed using the Fourier-based reconstruction algorithm with 50 iterations. The reconstructed 3D volume was segmented and refined by threshold segmentation and Gaussian filter in MATLAB. The porosity can be calculated as follows: porosity = V_{frame}/$V_{total} \times 100\%$. Where V_{frame} is the reconstructed 3D body for binarised acquisition, and V_{total} is the total volume of the reconstructed 3D body following the implementation of hole-filling techniques.

Electrochemical measurements

The catalyst ink was prepared by mixing 350 μL of H_2O, 100 μL of isopropanol, 50 μL of Nafion solution (5 wt% in isopropanol), and 5 mg of catalyst together, and then ultrasonic treatment for 1 h. Then, based on the zinc content, a certain volume of the ink was evenly loaded on the two sides of a carbon paper (1.0 × 1.0 cm²) to obtain a metal loading of 1 mg cm^{-2}. All the electrochemical measurements were conducted on the CHI760E electrochemical workstation (Shanghai Chen-Hua Instrument Corporation, China) and tested in a proton exchange membrane (Nafion®117) separated H-type cell by using a typical three-electrode system. Pt mesh and Hg/HgO (1 M KOH) electrodes were used as the counter and reference electrodes, respectively. The anodic compartment was filled with 15 mL of 0.7 M K_2CO_3 and 5 mL of a mixed solution of methanol and ammonia with different volume ratios. The cathodic compartment was filled with 20 mL of 0.7 M K_2CO_3. The linear sweep voltammetry (LSV) polarization curves were

measured at a scan rate of 10.0 mV s^{-1}. All curves were gained without IR compensation. All electrochemical measurements were performed at ambient temperature (25 °C) and pressure.

Calculation of Faradaic efficiency and electron efficiency

Assuming that the formation of a DMF molecule demands six electrons and one TMDM requires two electrons, the Faradaic efficiency (FE) can be calculated as follows: FE (%) = $100znF/Q$. Where z is the number of electrons required to form a molecule of product, n is the mole of product formed, F is the Faraday constant (96485 C mol^{-1}), and Q is the electric quantity. The electron efficiency (EE) is calculated as follows: EE (%) = FE × Yield.

Synthesis of other N−C−N bonded organonitrogen compounds: *N,N′*-diethyl-*N,N′*-dimethylmethanediamine, *N,N,N′,N′*-tetra-ethylmethanediamine and dimorpholinomethane

Other N−C−N bonded organonitrogen compounds were synthesized according to the procedures for TMDM, with the use of different amines as the reagents. The cathodic compartment was filled with 20 mL of 0.7 M K$_2$CO$_3$, while the anodic compartment was filled with 15 mL of 0.7 M K$_2$CO$_3$, 1 mL of methanol, and 4 mL of 40 wt% amine solution. After electrolysis for 3 h at 0.8 V, the electrolytes were extracted with dichloromethane, and the products were quantified by GC.

Synthesis of the organonitrogen compounds with (dimethyla-mino)methyl substituent

2-[(Dimethylamino)methyl]phenol. Following electrolysis, the electrolyte was extracted with 5 mL of trichloromethane and dried with anhydrous sodium sulfate. The resulting solution was then added to a single-necked flask with 94.1 mg (1 mmol) of phenol and 4.04 mg (0.04 mmol) of CuCl and stirred at 50 °C for 12 h. The product was quantified by GC. Yield: 56 mg (72%). ^{1}H NMR (600 MHz, DMSO-d_6): δ 7.13-6.98 (m, 2H), 6.72 (dd, J = 9.3, 5.1 Hz, 2H), 3.55 (s, 2H), 2.22 (s, 6H).

1-[(Dimethylamino)methyl]-2-naphthalenol. Following electrolysis, the electrolyte was extracted with 5 mL of trichloromethane and dried with anhydrous sodium sulfate. The resulting solution was then added to a single-necked flask with 169 mg (1.17 mmol) of 2-naphthol, 8 mg of K$_2$CO$_3$, and refluxed at 60 °C for 6 h. The resulting solution was extracted with 1 M HCl, and then the pH was adjusted to 8 by the addition of K$_2$CO$_3$. The precipitated solid was filtered and dried, resulting in the product. Yield: 204 mg (86%). ^{1}H NMR (600 MHz, DMSO-d_6): δ 7.93 (d, J = 5.7 Hz, 1H), 7.77 (d, J = 5.4 Hz, 1H), 7.70 (d, J = 5.9 Hz, 1H), 7.42 (t, J = 5.1 Hz, 1H), 7.26 (t, J = 4.9 Hz, 1H), 7.06 (d, J = 5.9 Hz, 1H), 3.98 (s, 2H), 2.29 (s, 6H); HRMS (*m/z*): [M + H]$^+$ calcd. for C$_{13}$H$_{16}$NO, 202.1154; found, 202.1235.

N,N-dimethyl-1-1,2,4-triazol-1-methanamine. Following electrolysis, the electrolyte was extracted with 5 mL of toluene and dried with anhydrous sodium sulfate. The resulting solution was then added to a single-necked flask with 69.1 mg (1 mmol) of 1,2,4-triazole, 1 mg of Pd(acac)$_2$, and refluxed at 90 °C for 4 h. Subsequently, after filtration, the product was obtained by rotary evaporation of the filtrate. Yield: 108 mg (85%). ^{1}H NMR (600 MHz, DMSO-d_6): δ 8.55 (s, 1H), 7.97 (s, 1H), 4.98 (s, 2H), 2.19 (s, 6H). HRMS (*m/z*): [M-C$_2$H$_2$N$_3$]$^+$ calcd. for C$_3$H$_8$N, 58.0675; found, 58.0500.

N,N-dimethyl-1H-imidazole-1-methanamine. Following electrolysis, the electrolyte was extracted with 15 mL of trichloromethane and dried with anhydrous sodium sulfate. The resulting solution was then added to a single-necked flask with 138 mg (2 mmol) of imidazole, 152 mg (1.1 mmol) of K$_2$CO$_3$, and 111 mg (1.1 mmol) of succinic anhydride, and the mixture was stirred at room temperature for 1 h. After reaction, 50 mL of trichloromethane was added, and the organic phase was washed with 1 M NaOH and saturated NaCl solution, respectively. The

organic phase was then dried with anhydrous sodium sulfate, and the resulting product was obtained by rotary evaporation. Yield: 94 mg (94%). ^{1}H NMR (600 MHz, DMSO-d_6): δ 7.62 (s, 1H), 7.15 (s, 1H), 6.90 (s, 1H), 4.73 (s, 2H), 2.15 (s, 6H). HRMS (*m/z*): [M + H]$^+$ calcd. for C$_5$H$_{11}$N$_4$, 125.175; found, 126.1013.

Topotecan hydrochloride. Following electrolysis, the electrolyte was extracted with 5 mL of trichloromethane and dried with anhydrous sodium sulfate. The extracts from six electrolysis batches were combined and added to a single-necked flask, together with 1.00 g (2.69 mmol) of 10-hydroxycamptothecin. The mixture was then stirred at 45 °C for 24 hours. After the reaction, the solid was obtained by rotary evaporation. The solid was dissolved in 20 mL of 0.4 M HCl and stirred at room temperature for 16 hours. The resulting solution was filtered and freeze-dried to obtain the product. Yield: 1.16 g (95%). ^{1}H NMR (600 MHz, DMSO-d_6): δ 9.82 (s, 1H), 8.98 (s, 1H), 8.17 (d, J = 6.2 Hz, 1H), 7.72 (d, J = 6.1 Hz, 1H), 7.28 (s, 1H), 6.53 (s, 1H), 5.42 (s, 2H), 5.26 (s, 2H), 4.72 (s, 2H), 2.83 (s, 6H), 1.87 (m, J = 14.2, 9.4, 4.8 Hz, 2H), 0.88 (t, J = 4.9 Hz, 3H); UV/Vis: λmax 225 nm; HRMS (*m/z*): [M−Cl]$^+$ calcd. for C$_{23}$H$_{24}$N$_3$O$_5$, 422.1710; found, 422.1706.

3-(((4-ethyl-4,9-dihydroxy-3,14-dioxo-3,4,12,14-tetrahydro-1H pyr-ano[3′,4′:6,7]indolizino[1,2-b]quinolin-10 yl)methyl)dimethylammo-nio)propane-1-sulfonate (Sulfonate functionalized topotecan). Topotecan hydrochloride (0.2 mmol, 92 mg) was combined with 5 mL of trichloromethane and 24.4 mg (0.2 mmol) of 1,3-propanesulfonate, and refluxed at 80 °C for 36 h. After the reaction, the solid was obtained by rotary evaporation at 45 °C. The solid was continuously rinsed with trichloromethane, dispersed in trichloromethane, ultrasonicated to dissolve a small number of impurities, filtered, and dried to obtain the product. Yield: 80 mg (74%). ^{1}H NMR (600 MHz, DMSO-d_6): δ 9.39 (s, 1H), 8.93 (s, 1H), 8.18 (d, J = 6.1 Hz, 1H), 7.64 (d, J = 6.1 Hz, 1H), 7.29 (s, 1H), 6.53 (s, OH), 5.42 (s, 2H), 5.27 (s, 2H), 4.73 (s, 2H), 3.71 (t, J = 4.5 Hz, 2H), 2.85 (s, 6H), 2.53 (t, 2H), 2.0 (m, 2H), 1.87 (m, J = 14.2, 9.5, 4.7 Hz, 2H), 0.88 (t, J = 4.8 Hz, 3H); ^{13}C NMR (150 MHz, DMSO-d_6): δ 172.64, 156.98, 156.94, 150.18, 149.66, 145.59, 143.47, 133.22, 130.68, 129.09, 126.55, 122.18, 118.67, 108.50, 96.28, 72.51, 65.33, 50.62, 50.35, 48.57, 44.85, 42.65, 30.32, 28.97, 7.89; HRMS (*m/z*): [M−C$_3$H$_7$O$_3$S]$^+$ calcd. for C$_{23}$H$_{24}$N$_3$O$_5$, 422.1710; found, 422.1709.

Product quantification and identification

After electrolysis, the electrolyte was divided into two parts and extracted by dichloromethane and 1,2-dichlorobenzene, respectively. Dichloromethane extract was used for the detection of DMF, and 1,2-dichlorobenzene extract was used for the detection of TMDM. The final samples were further identified by GC-MS (Shimadzu GCMS-QP2020) and quantified by GC (Shimadzu GC-2018). Formate was quantified by ^{1}H nuclear magnetic resonance (^{1}H NMR) (ECZ600R, 600 MHz) using H$_3$BTC as the internal standard. In detail, the mixture of 500 μL of electrolyte and 100 μL of D$_2$O containing 10 mM H$_3$BTC solution was used as the test sample.

Computational details for calculations

First-principles calculations based on density functional theory (DFT) were conducted using the Vienna ab initio Simulation Package (VASP). The projector augmented wave (PAW) method was employed to solve the Kohn-Sham equations, while the Perdew-Burke-Ernzerhof (PBE) generalized gradient approximation (GGA) described exchange-correlation interactions. The van der Waals interactions were incorporated into the standard DFT framework via the DFT-D3 dispersion correction. A 15 Å vacuum layer was introduced to eliminate the interaction between the periodically repeated structures. In this work, key computational parameters included: a 400 eV plane-wave cutoff energy, a 2 × 2 × 1 Monkhorst-Pack k-point grid, and convergence criteria of 10^{-5} eV (energy) and 0.05 eV Å^{-1} (residual forces). The density of

states (DOS) was computed with Gaussian smearing (0.1 eV width). Free energy diagrams were generated via the computational hydrogen electrode (CHE) method. The Gibbs free energies were calculated at 298 K and 1 atm according to $G = E + E_{ZPE} - TS$, where E is the total energy, E_{ZPE} is the zero-point vibrational energy, T is the absolute temperature, and S is the entropy.

Data availability

The data supporting the findings of this study are available within the article and the Supplementary Information, and can also be obtained from the corresponding author upon reasonable request. The material characterizations and electrocatalytic performance data generated in this study have been deposited in the Figshare database https://doi.org/10.6084/m9.figshare.28522397.

References

1. Akita, M., Ceroni, P., Stephenson, C. R. J. & Masson, G. Progress in photocatalysis for organic chemistry. *J. Org. Chem.* **88**, 6281–6283 (2023).
2. Narayanam, J. M. R. & Stephenson, C. R. J. Visible light photoredox catalysis: applications in organic synthesis. *Chem. Soc. Rev.* **40**, 102–113 (2011).
3. Yang, L. et al. Thermal nickel-catalyzed carbon–oxygen cross-coupling of (hetero)aryl halides with alcohols enabled by the use of a silane reductant approach. *ACS Catal.* **14**, 7846–7852 (2024).
4. Zhang, J. et al. Recent advances in C(sp3)–N bond formation via metallaphoto-redox catalysis. *Chem. Commun.* **60**, 6340–6361 (2024).
5. Li, J. et al. Heterogeneous electrosynthesis of C–N, C–S and C–P products using CO_2 as a building block. *Nat. Synth.* **3**, 809–824 (2024).
6. Wang, Y. et al. Electrochemical late-stage functionalization. *Chem. Rev.* **123**, 11269–11335 (2023).
7. Anastasiadou, D. & Costa Figueiredo, M. Electrocatalytic pathways to the formation of C–N bonds. *ACS Catal.* **14**, 5088–5097 (2024).
8. Peng, X. et al. Electrochemical C–N coupling of CO_2 and nitrogenous small molecules for the electrosynthesis of organonitrogen compounds. *Chem. Soc. Rev.* **52**, 2193–2237 (2023).
9. Schiffer, Z. J. & Manthiram, K. Electrification and decarbonization of the chemical industry. *Joule* **1**, 10–14 (2017).
10. Zhu, C., Ang, N. W. J., Meyer, T. H., Qiu, Y. & Ackermann, L. Organic electrochemistry: molecular syntheses with potential. *ACS Cent. Sci.* **7**, 415–431 (2021).
11. Shih, C. F., Zhang, T., Li, J. & Bai, C. Powering the future with liquid sunshine. *Joule* **2**, 1925–1949 (2018).
12. Zhong, J. W. et al. State of the art and perspectives in heterogeneous catalysis of CO_2 hydrogenation to methanol. *Chem. Soc. Rev.* **49**, 1385–1413 (2020).
13. Tang, H.-T., Pan, Y.-Z. & Pan, Y.-M. Research progress in electrochemical/photochemical utilization of methanol as a C1 source. *Green. Chem.* **25**, 8313–8327 (2023).
14. Meng, N. et al. Electrosynthesis of formamide from methanol and ammonia under ambient conditions. *Nat. Commun.* **13**, 5452 (2022).
15. Li, W. et al. Sustainable electrosynthesis of N,N-Dimethylformamide via relay catalysis on synergistic active sites. *J. Am. Chem. Soc.* **146**, 21968–21976 (2024).
16. Yamaguchi, K., Kobayashi, H., Oishi, T. & Mizuno, N. Heterogeneously catalyzed synthesis of primary amides directly from primary alcohols and aqueous ammonia. *Angew. Chem. Int. Ed.* **51**, 544–547 (2012).
17. Shao, J. et al. Scalable electrosynthesis of formamide through C–N coupling at the industrially relevant current density of 120 mA cm^{-2}. *Angew. Chem. Int. Ed.* **61**, e202213009 (2022).
18. Xia, R. et al. Electrosynthesis of ethylene glycol from C(1) feedstocks in a flow electrolyzer. *Nat. Commun.* **14**, 4570 (2023).
19. Yeo, J. B., Jang, J. H., Jo, Y. I., Koo, J. W. & Nam, K. T. Paired electrosynthesis of formaldehyde derivatives from CO_2 reduction and methanol oxidation. *Angew. Chem. Int. Ed.* **63**, e202316020 (2024).
20. Jang, J. H. et al. Electrochemically initiated synthesis of ethylene carbonate from CO_2. *Nat. Synth.* **3**, 846–857 (2024).
21. DeSolms, S. J. N,N,N′,N′-Tetramethylmethanediamine. A simple, effective Mannich reagent. *J. Org. Chem.* **41**, 2650–2651 (1976).
22. Mazurkiewicz, R., Październiok-Holewa, A., Adamek, J. & Zielińska, K. Chapter two-α-amidoalkylating agents: Structure, synthesis, reactivity and application. In: *Advances in Heterocyclic Chemistry* (ed Katritzky, A. R.) (Academic Press, 2014).
23. Puri, S. C., Handa, G., Dhar, K. L., Suri, O. P. & Qazi, G. N. Aminoalkylation of 10-Hydroxycamptothecin using methylene chloride under solid–liquid phase transfer catalysis: a new approach for the preparation of topotecan. *Synth. Commun.* **34**, 2857–2862 (2004).
24. Wu, G. et al. Emerging electrocatalysts in urea production. *Chem. Eur. J.* **29**, e202301619 (2023).
25. Chen, C. et al. Local reaction environment in electrocatalysis. *Chem. Soc. Rev.* **53**, 2022–2055 (2024).
26. Seh, Z. W. et al. Combining theory and experiment in electrocatalysis: Insights into materials design. *Science* **355**, eaad4998 (2017).
27. Deng, Z. et al. Electrocatalytic organic transformation reactions in green chemistry: exploring nanocrystals and single atom catalysts. *Nano Res.* **17**, 9326–9344 (2024).
28. Wang, A. Q., Li, J. & Zhang, T. Heterogeneous single-atom catalysis. *Nat. Rev. Chem.* **2**, 65–81 (2018).
29. Chen, Y. et al. Single-atom catalysts: synthetic strategies and electrochemical applications. *Joule* **2**, 1242–1264 (2018).
30. Han, L. et al. Stable and efficient single-atom Zn catalyst for CO_2 reduction to CH_4. *J. Am. Chem. Soc.* **142**, 12563–12567 (2020).
31. Yang, F. et al. Highly efficient CO_2 electroreduction on ZnN_4–based single–atom catalyst. *Angew. Chem. Int. Ed.* **57**, 12303–12307 (2018).
32. Li, S. et al. Low–valence $Zn^{\delta+}$ (0<δ<2) single–atom material as highly efficient electrocatalyst for CO2 reduction. Angew. Chem. *Int. Ed.* **60**, 22826–22832 (2021).
33. He, Y.-C. et al. Integrated 3D open network of interconnected bismuthene arrays for energy-efficient and electrosynthesis-assisted electrocatalytic CO_2 reduction. *Small* **18**, 2105246 (2022).
34. Xin, S. et al. Electron delocalization realizes speedy fenton-like catalysis over a high-loading and low-valence zinc single-atom catalyst. *Adv. Sci.* **10**, 2304088 (2023).
35. Lei, J., Sun, X., Jin, Y., Xu, C. & Li, B. Atomic dispersion of Zn^{2+} on N-Doped carbon materials: from non-activity to high activity for catalyzing luminol-H_2O_2 chemiluminescence. *Anal. Chem.* **94**, 17559–17566 (2022).
36. Jiao, L. et al. Hierarchically ordered porous superstructure embedded with readily accessible atomic pair sites for enhanced CO_2 electroreduction. *Appl. Catal. B* **330**, 122638 (2023).
37. Wang, N. et al. Ordered macroporous superstructure of bifunctional cobalt phosphide with heteroatomic modification for paired hydrogen production and polyethylene terephthalate plastic recycling. *Appl. Catal. B* **316**, 121667 (2022).
38. Li, X., Wu, X.-T., Xu, Q. & Zhu, Q.-L. Hierarchically ordered pore engineering of metal–organic framework-based materials for electrocatalysis. *Adv. Mater.* **36**, 2401926 (2024).
39. Chen, J. et al. Promoting CO_2 electroreduction kinetics on atomically dispersed monovalent ZnI sites by rationally engineering proton-feeding centers. *Angew. Chem. Int. Ed.* **61**, e202111683 (2021).
40. Wei, Y. et al. Atomically dispersed zinc active sites efficiently promote the electrochemical conversion of N_2 to NH_3. *Energy Environ. Mater.* **7**, e12630 (2023).
41. Lu, Z. et al. Zinc single-atom-regulated hard carbons for high-rate and low-temperature sodium-ion batteries. *Adv. Mater.* **35**, 2211461 (2023).

42. Dong, C. et al. Hollow carbon sphere nanoreactors loaded with PdCu nanoparticles: void-confinement effects in liquid-phase hydrogenations. *Angew. Chem. Int. Ed.* **59**, 18374–18379 (2020).

43. Tian, H. et al. The development of yolk–shell-structured Pd&ZnO@carbon submicroreactors with high selectivity and stability. *Adv. Funct. Mater.* **28**, 1801737 (2018).

44. Zhou, Z. et al. Porphyrinic MOF derived single-atom electrocatalyst enables methanol oxidation. *Chem. Eng. J.* **449**, 137888 (2022).

45. Ruan, J. et al. Cobalt single atoms enabling efficient methanol oxidation reaction on platinum anchored on nitrogen-doped carbon. *Small* **18**, 2107067 (2022).

46. Kaur, J. et al. Single-atom catalysts for oxygen reduction reaction and methanol oxidation reaction. *Fuel* **358**, 130241 (2024).

47. Xiao, R., Ye, J., Li, X. & Wang, X. Dual size/charge-switchable and multi-responsive gelatin-based nanocluster for targeted anti-tumor therapy. *Int. J. Biol. Macromol.* **238**, 124032 (2023).

48. Fan, Y. et al. Electrochemical synthesis of formamide by C–N coupling with amine and CO_2 with a high faradaic efficiency of 37.5. *Chem* **10**, 2437–2449 (2024).

49. Jin, M. et al. Electrosynthesis of N,N-dimethylformamide from market-surplus trimethylamine coupled with hydrogen production. *Green. Chem.* **25**, 5936–5944 (2023).

50. Möhlmann, G. R. Raman spectra of aqueous solutions of formaldehyde and its oligomers. *J. Raman Spectrosc.* **18**, 199–203 (1987).

51. Yang, H. et al. Intermediates adsorption engineering of CO_2 electroreduction reaction in highly selective heterostructure Cu-based electrocatalysts for CO production. *Adv. Energy Mater.* **9**, 1970107 (2019).

Acknowledgements

Author contributions

D.M. and Q.Z. conceived and designed the idea. Y.H. conducted the experiments, and X.L. assisted in the synthesis of catalysts. K.M. and L.H. assisted with the 3D TEM tomography tests. D.M., X.W., Q.Z., and Y.H. discussed the results and prepared the manuscript. All the authors reviewed the manuscript.

Competing interests

The authors declare no competing interests.

Additional information

Supplementary information The online version contains supplementary material available at https://doi.org/10.1038/s41467-025-58948-3.

Correspondence and requests for materials should be addressed to Qi-Long Zhu.

Peer review information *Nature Communications* thanks Yang Hou, Nikolay Kornienko, Shuangyin Wang and the other, anonymous, reviewer(s) for their contribution to the peer review of this work. A peer review file is available.

Reprints and permissions information is available at http://www.nature.com/reprints

Publisher's note Springer Nature remains neutral with regard to jurisdictional claims in published maps and institutional affiliations.